

Research Papers

Optimizing EMIMBF₄-based electrolyte with LiBr redox medium for enhanced supercapacitors



Zhemin Li, Dewei Xiao, Zihan Li, Zhenming Xu, Hui Dou, Xiaogang Zhang*

Jiangsu Key Laboratory of Electrochemical Energy Storage Technologies, College of Materials Science and Technology, Nanjing University of Aeronautics and Astronautics, Nanjing 210016, China

ARTICLE INFO

Keywords:
Supercapacitors
Redox electrolyte
Ionic liquid
Organic solvent

ABSTRACT

The formidable challenge of supercapacitors (SCs) is to achieve both high energy density and high power density simultaneously. Although the utilization of porous carbon materials for physical adsorption in electrochemical double-layer capacitors (EDLCs) applications exhibits promising prospects, attaining exceptional performance necessitates additional methodologies. Here, we propose an effective strategy for formulating redox electrolytes through the incorporation of organic solvents and LiBr into 1-ethyl-3-methylimidazole tetrafluoroborate (EMIMBF₄) electrolytes. Within this formulation, LiBr serves as a redox mediator, contributing Br⁻/Br₃⁻ redox pairs to the system. The incorporation of EMIMBF₄-LiBr-DMSO in brominated redox EDLCs led to a significant enhancement in specific capacitance, reaching up to 39.72 F g⁻¹, representing a remarkable increase of 159 % compared to EDLCs without any redox media. This configuration achieved a high power density of 496.6 W kg⁻¹ while maintaining an energy density of 34.48 Wh kg⁻¹.

1. Introduction

As people's living standards continue to rise, the requirements for energy storage equipment are becoming higher. Electrochemical double-layer capacitors (EDLCs), also referred to as supercapacitors (SCs), have garnered significant attention in the realm of energy storage due to their excellent cycle life and high power density [1–3]. In general, EDLCs facilitate charge storage through physical adsorption on the surface of carbon electrodes, enabling rapid energy storage [4]. Therefore, ion–carbon interactions, ion–ion interactions and the size of ions all affect the diffusion rate of ions in the electrode. However, the relatively low energy density of SCs limits their market share, posing a significant challenge to their widespread commercialization [5]. Since the energy density of EDLC is proportional to the specific capacitance multiplied by the square of the operating potential, the strategy to increase the energy density of EDLC is to enlarge the voltage window of the electrolyte and improve the effective utilization of the surface of electroactive material [6].

To optimize the utilization of the electrode surface, researchers have strived to increase its specific surface area through the synthesis of a variety of high-capacity nanomaterials, encompassing activated carbon (AC) [7–9], carbon nanotubes (CNTs) [10–12], and graphene [13–15].

Additionally, they have incorporated active functional groups such as nitrogen and oxygen onto the surface of carbon materials to enhance redox capacitance. Among the various transition metal oxides currently available, ruthenium dioxide (RuO₂) exhibits the highest specific capacitance [16]. However, its commercial application is limited due to its high cost. Furthermore, electrode materials with redox activity face certain challenges such as significantly lower electrical conductivity, partial irreversibility of chemical reactions, and relatively shorter lifespan compared to carbon materials.

In addition to the electrode materials, the electrolyte is a crucial factor determining the performance of SCs. The energy density can be significantly increased by expanding the voltage window, which largely depends on the choice of electrolyte [17]. Therefore, organic electrolytes and ionic liquids capable of achieving a wide voltage window (>3–4 V) are preferred for manufacturing high-performance energy storage devices. Ionic liquids (ILs) have gained attention in electrolyte systems due to their high chemical and electrochemical stability, as well as safety features. ILs, a type of molten salt with organic cations and organic/inorganic anions, show spontaneous ion filling in carbon nanopores without external electric fields [18]. Despite the increased operational voltage observed in supercapacitors based on pure ionic liquids, several challenges persist due to issues such as heightened viscosity, reduced ion

* Corresponding author.

E-mail address: azhangxg@nuaa.edu.cn (X. Zhang).

conductivity, and compromised device rate performance and cycling stability.

The incorporation of organic solvents into ionic liquids can mitigate the limitations associated with pure ionic liquids, thereby reducing viscosity and improving ion conductivity. Lewandowski et al. reported a notable enhancement in the room temperature conductivity of *N*-methyl-*n*-propyl piperidinium bis(trifluoromesulfonyl) imide(MePr-PipTFSI) when 52 % acetonitrile was added, with the conductivity increasing from 1.5 mS cm^{-1} to 40 mS cm^{-1} [19]. Ruiz et al. reported that the specific capacity of EDLCs using a mixture of *n*-butyl-*n*-methylpyrrole bis(trifluoromethyl-sulfonyl) imide salt (PYR₁₄TFSI) and nitrile as an electrolyte was higher compared to that of EDLC utilizing pure PYR₁₄TFSI [20]. However, Palm et al. discovered that the utilization of a blend of organic solvents (such as acetonitrile, propylene carbonate, and γ -butyrolactone) in conjunction with 1-ethyl-3-methylimidazolium tetrafluoro-borate (EMIMBF₄) as the electrolyte for EDLCs not only reduces the viscosity and melting point of EMIMBF₄ while enhancing ion conductivity but also exerts certain adverse effects on the electrochemical performance of EDLCs [21]. Therefore, one of the significant challenges in the application of ionic liquids in SCs is to incorporate organic solvents without compromising the inherent advantages of pure ionic liquids.

The addition of a redox medium to the electrolyte facilitates rapid and reversible redox reactions, thereby effectively enhancing both ionic conductivity and pseudocapacitance. Redox supercapacitors utilize soluble redox medium for additional capacity, requiring stable, reversible, appropriately redox-potential materials with rapid kinetic reactions. The kinetics involve the diffusion rate, solvation/desolvation rate of the redox medium in solution, as well as the interaction between the redox medium and the electrode, encompassing adsorption/desorption rate and charge transfer rate. Since the redox reaction during the device operation mainly occurs at the electrode/electrolyte interface, the volume expansion of the electrode material caused by ion insertion or alloying can be avoided. Representative redox mediators include hydroquinone [22–25], viologen [26–29], Fe³⁺/Fe²⁺ [30–33], Zn²⁺ [34], I[−]/I₃[−] [35–38], and Br[−]/Br₃[−] [39,40], NH₄⁺/H⁺ [41]. Among them, the Br[−]/Br₃[−] redox mediator exhibits a high scale quasi-potential (1.07 V vs. SHE), excellent solubility, and rapid reaction kinetics.

In this study, 1-ethyl-3-methylimidazole tetrafluoroborate (EMIMBF₄) was chosen as the selected ionic liquid, lithium bromide (LiBr) served as the redox medium, while acetonitrile (ACN), propylene carbonate (PC), and dimethyl sulfoxide (DMSO) were utilized as organic solvents for preparing the redox electrolyte, respectively. The bromine-based redox EDLCs was fabricated using activated carbon as the electrode material. Through theoretical calculations, the unique solvent-solute interactions between Br ions and various organic solvents in the system were revealed, ultimately determining that DMSO is the optimal organic solvent for Br-based redox EDLCs. The Br-based redox supercapacitor, constructed with EMIMBF₄-LiBr-DMSO electrolyte, demonstrates exceptional electrochemical performance. It exhibits a remarkable specific capacitance of 39.72 F g^{-1} , which is 159 % higher than that of the EDLCs without the utilization of a redox medium. Moreover, this device achieves an impressive power density of 496.6 W kg^{-1} while maintaining an energy density of 34.48 Wh kg^{-1} .

2. Experimental

2.1. Materials

The 1-ethyl-3-methylimidazole tetrafluoroborate (EMIMBF₄) was procured from Suzhou Duo Duo Chemical Co., LTD. Acetonitrile (ACN), dimethyl sulfoxide (DMSO), and lithium bromide (LiBr) were obtained from Shanghai Aladdin Technology Co., LTD. Propylene carbonate (PC), Polytetrafluoroethylene (PTFE), and acetylene Black (ACET) were sourced from Nanjing Chemical Reagent Co., LTD. YP-50F activated carbon was purchased from Kuraray Chemical Company.

2.2. Preparation of redox electrolyte

The preparation of the electrolyte solution involved in this work was carried out in the glovebox filled with Ar atmosphere ($\text{H}_2\text{O} < 0.1 \text{ ppm}$, $\text{O}_2 < 0.1 \text{ ppm}$). 10 mL of organic solvents (propylene carbonate (PC), acetonitrile (ACN), and dimethyl sulfoxide (DMSO)) were individually dispensed. Subsequently, 1 M LiBr and 1 M EMIMBF₄ were introduced into each respective solvent. The hybrid solutions, namely EMIMBF₄-LiBr-PC, EMIMBF₄-LiBr-ACN, and EMIMBF₄-LiBr-DMSO, were obtained through stirring at room temperature with a speed of 300 rpm until achieving a homogeneous colorless solution.

2.3. Preparation of active carbon electrode

Firstly, a mixture of YP-50F activated carbon, acetylene black, and polytetrafluoroethylene in a ratio of 8:1:1 (with YP-50F activated carbon at 1 mg) is prepared. The slurry is thoroughly mixed with anhydrous ethanol to ensure uniformity. Subsequently, the slurry is evenly coated onto a stainless steel mesh and subjected to vacuum drying at 110°C for 12 h. Finally, it is pressed under a pressure of 10 MPa. The tap density is 1.54 g cm^{-3} .

2.4. Characterization methods

The viscosity and conductivity of the prepared redox electrolyte were measured using an NDJ series digital viscometer (NDJ—5S) and a DDSJ-318 conductivity meter, respectively. The wettability of the electrolyte and electrode was evaluated using a JC2000D1 contact angle measuring instrument. According to the contact angle formula:

$$\gamma_{SV} = \gamma_{SL} + \gamma_{LV} \times \cos\theta \quad (1)$$

The smaller θ proves that the liquid wets the solid more easily, indicating that the wettability is better. If θ is larger, the wettability is worse (where γ_{SV} , γ_{SL} , γ_{LV} are the solid-gas interface, solid-liquid interface, and the liquid-gas interface, respectively, and θ is the contact angle).

Raman spectra was recorded using a HORIBA Scientific LabRAMHR Raman spectrometer system equipped with a 532 nm laser. Nitrogen adsorption-desorption isotherms at 77 K were obtained using an ASAP 2460 physical adsorption analyzer to analyze the specific surface area and pore size distribution of activated carbon electrodes. The surface functional groups of the cycled activated carbon electrode were characterized by FT-IR (Bruker IFS66 v/S) in the range of 500–4000 cm^{-1} . X-ray photoelectron spectroscopy (XPS) with Al K α (1486.6 eV) as the X-ray source, specifically Perkin-Elmer PHI 550, was employed to investigate changes in the valence state of activated carbon electrodes after cycling.

2.5. Electrochemical tests

The carbon-based symmetric supercapacitors were assembled in a glove compartment under the protection of argon gas. The activated carbon electrode, prepared as described above, was utilized as both the positive and negative electrodes, while Whatman GF/A glass fiber served as the separator. And various redox electrolytes were incorporated to assemble the CR2016 button battery. Electrochemical impedance spectroscopy (EIS), constant current charge and discharge (GCD), and cyclic voltammetry (CV) tests were performed on the Biologic VMP-300 electrochemical workstation, and cyclic charge and discharge tests were performed on the CT2001A blue battery. EIS tests were performed at open circuit potential with an amplitude of 5 mV and a frequency range of 10 mHz to 100 kHz.

The mass specific capacitance of the capacitor device can be calculated from the GCD curves:

$$C_m = (I \Delta t) / (m \Delta V) \quad (2)$$

The C_m is defined as the mass-specific capacitance of a device (F g^{-1}), where I , Δt , m , and ΔV represent the current density (A), discharge time (s), total mass of positive and negative carbon materials (g), and voltage window (V), respectively.

The energy density (E , Wh kg^{-1}) and power density (P , W kg^{-1}) of a supercapacitor can be calculated by the following formula:

$$E = C_m V^2 / (2 * 3.6) \quad (3)$$

$$P = 3600E / \Delta t \quad (4)$$

2.6. Theoretical calculations

Three models of electrolytes were developed to simulate EMIMBF₄-LiBr-PC, EMIMBF₄-LiBr-ACN, and EMIMBF₄-LiBr-DMSO electrolytes. The composition of the EMIMBF₄-LiBr-PC model includes 20 EMIMBF₄, 20 LiBr, and 380 PC molecules, while the EMIMBF₄-LiBr-ACN model comprises of 20 EMIMBF₄, 20 LiBr, and 280 ACN molecules and the EMIMBF₄-LiBr-LiBr model comprises of 20 EMIMBF₄, 20 LiBr, and 220 DMSO molecules. Additionally, a fixed time step of 1 fs was implemented. The electrolyte systems were stabilized in the isothermal-isobaric ensemble (constant NPT) by employing the Berendsen barostat, which effectively regulated the pressure at 0.1 MPa over a duration of 100 ps using a decay constant of 0.1 ps. The Nose thermostat was utilized to maintain a temperature of 298 K. Subsequently, a production run lasting 100 ps was conducted in the canonical ensemble (NVT) at the same temperature. The simulation duration was sufficiently extended to guarantee attainment of equilibrium states for the electrolyte systems.

3. Results and discussion

3.1. Physical characteristics and structure of the electrolytes

The electrochemical stability of the electrolyte was evaluated by linear sweep voltammetry (LSV). Fig. 1a shows that the oxidation stability of all three electrolytes remains stable below 1.5 V. When the current changes significantly, it indicates that the electrolyte interface has undergone severe oxidation reactions, which is consistent with the oxidation potential of the electrolyte. Specifically, the EMIMBF₄-LiBr-PC and EMIMBF₄-LiBr-ACN electrolytes undergo oxidation reactions at 1.6 V and 3.4 V, respectively, while the EMIMBF₄-LiBr-DMSO electrolyte has a higher oxidation potential compared to the other two electrolytes, reaching 4.2 V, thereby achieving a wider voltage window. This means that when using EMIMBF₄-LiBr-DMSO as the electrolyte, stability can be maintained at higher voltages because it has a higher oxidation potential. Therefore, the presence of EMIMBF₄-LiBr-DMSO allows the electrolyte to withstand a wider voltage range. We characterized the vibrational properties of electrolytes using Raman spectroscopy, delving into the distinct solvation structures of the three electrolytes.

In the extensive frequency range of 2800 to 2963 cm⁻¹, the bands are attributed to the fingerprint region of symmetric and asymmetric C—H stretching in imidazolium cations [42]. The band observed at approximately 2950 cm⁻¹ corresponds to the vibration of CH₃ and was detected in all samples. This peak can be attributed to the existence of multiple CH₃ terminals within the structures. Another characteristic peak observed in all samples is found at the wavenumber range of 3078–3089 cm⁻¹, which can be attributed to the stretching vibration of C—H. Additionally, a peak around 3096 cm⁻¹ is assigned to the stretching

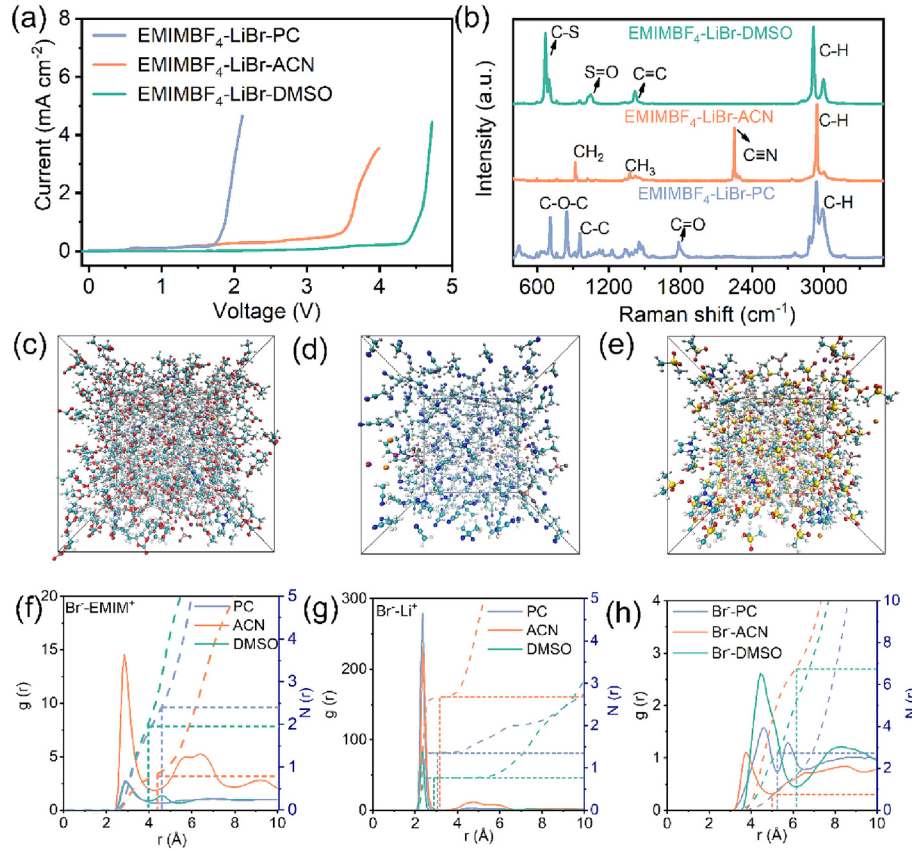


Fig. 1. (a) LSV curves of EMIMBF₄-LiBr-PC, EMIMBF₄-LiBr-ACN, and EMIMBF₄-LiBr-DMSO SCs. (b) Raman spectra of electrolytes and solvents. Characterization of the Br⁻ solvation structures of the designed electrolytes. Snapshots of MD simulation boxes for (c) EMIMBF₄-LiBr-PC, (d) EMIMBF₄-LiBr-ACN, and (e) EMIMBF₄-LiBr-DMSO. Radical distribution functions calculated from MD simulations of (f) Br⁻-EMIM⁺, (g) Br⁻-Li⁺, (h) Br⁻-PC, Br⁻-ACN, and Br⁻-DMSO pairs in Base. (Atom color: B, pink; Br, orange; F, gray; C, cyan; H, white; Li, purple; N, blue; O, red; S, yellow.) (For interpretation of the references to color in this figure legend, the reader is referred to the web version of this article.)

vibration of (C—H). The three electrolytes all demonstrate the capability to detect signals at $\sim 3159\text{ cm}^{-1}$, which corresponds to the HC=CH ring in EMIMBF₄. Due to the lower wavenumber of the C—H bond, it indicates a lower vibrational frequency, corresponding to longer bond length and weaker bond strength. By comparing the C—H bonds of three samples, it can be concluded that the C—H bond wavenumber in EMIMBF₄-LiBr-DMSO is the lowest, indicating that in this system, this chemical bond is more prone to breakage or participation in chemical reactions.

The solvation structure of bromide ions in three different electrolytes (EMIMBF₄-LiBr-PC, EMIMBF₄-LiBr-ACN, EMIMBF₄-LiBr-DMSO) were investigated through molecular dynamics (MD) simulations. Based on the MD snapshots, it can be observed that Br[−] is uniformly distributed in the three electrolytes. According to the analysis of the radial distribution function data of bromide ions in the EMIMBF₄-LiBr-PC solution, EMIMBF₄-LiBr-ACN electrolyte, and EMIMBF₄-LiBr-DMSO electrolyte in Fig. 1f-h, the coordination numbers (n) of Br[−]-(EMI⁺)_n, Br[−]-(Li⁺)_n, and Br[−]-(PC)_n in EMIMBF₄-LiBr-PC electrolyte are 2.4, 1.3, and 2.7, respectively. In EMIMBF₄-LiBr-ACN electrolyte, the coordination number (n) of Br[−]-(EMI⁺)_n is 0.8, Br[−]-(Li⁺)_n is 2.7, and Br[−]-(ACN)_n is 0.8. In EMIMBF₄-LiBr-DMSO electrolyte, the coordination numbers (n) of Br[−]-(EMI⁺)_n, Br[−]-(Li⁺)_n, and Br[−]-(DMSO)_n are 1.9, 0.7 and 6.7, respectively. In EMIMBF₄-LiBr-PC, EMIMBF₄-LiBr-ACN and EMIMBF₄-LiBr-DMSO electrolytes, the total coordination numbers of bromide ions are 6.4, 4.3 and 9.3, respectively. The increase in the coordination number between solvent molecules and bromine ions in the electrolyte will enhance the protection of solvent molecules, thereby decelerating the decomposition of the electrolyte at high voltage and expanding the operational voltage range.

The conductivity and viscosity of three redox electrolytes, namely 1 M EMIMBF₄ + 1 M LiBr + PC (EMIMBF₄-LiBr-PC), 1 M EMIMBF₄ + 1 M LiBr + ACN (EMIMBF₄-LiBr-ACN), and 1 M EMIMBF₄ + 1 M LiBr + DMSO (EMIMBF₄-LiBr-DMSO), was measured using the conductivity meter and viscometer. Fig. S1a shows conductivity and viscosity of EMIMBF₄-LiBr-PC, EMIMBF₄-LiBr-ACN, and EMIMBF₄-LiBr-DMSO. The conductivities of EMIMBF₄-LiBr-PC, EMIMBF₄-LiBr-ACN and EMIMBF₄-LiBr-DMSO are 8.24 mS cm^{−1}, 32.24 mS cm^{−1} and 12.34 mS cm^{−1}, respectively. Among the three redox electrolyte systems, the ACN system demonstrates superior ionic conductivity compared to other solvent systems. The low viscosity, small molecular radius and moderate dielectric constant of ACN may be attributed to its specific parameters (refer to Table S1). The viscosities of EMIMBF₄-LiBr-PC, EMIMBF₄-LiBr-ACN and EMIMBF₄-LiBr-DMSO were 7.62 mPa s, 1.10 mPa s, and 5.88 mPa s respectively. The order of the viscosities of the three redox electrolytes is EMIMBF₄-LiBr-PC > EMIMBF₄-LiBr-DMSO > EMIMBF₄-LiBr-ACN, which is consistent with the order of the viscosities of the three organic solvents PC > DMSO > ACN in Table S1. The contact angles of the three redox electrolytes and carbon materials were tested with a contact angle tester, as shown in Fig. S1b. The contact angles of EMIMBF₄-LiBr-PC, EMIMBF₄-LiBr-ACN and EMIMBF₄-LiBr-DMSO are 44.80°, 37.90° and 69.78°, respectively. Therefore, these three redox electrolytes were effective in wetting carbon materials. If θ is larger, the wettability is worse, which indicates that the order of wettability of the three redox electrolytes to carbon materials is EMIMBF₄-LiBr-ACN > EMIMBF₄-LiBr-PC > EMIMBF₄-LiBr-DMSO.

3.2. Electrochemical performance

Firstly, the carbon-based symmetric supercapacitors were fabricated by utilizing activated carbon as the electrode and, PC, ACN, and DMSO as organic electrolytes respectively, while incorporating 1 M LiBr as the redox mediator. The CV curves of the 1 M LiBr-PC supercapacitor with a scanning rate of 10 mV s^{−1}, as depicted in Fig. S2a, exhibits a rectangular shape at 1.2 V, indicating the exclusive presence of double-layer capacitance behavior. However, as the voltage range gradually extends to 2.0 V, polarization becomes evident at higher potentials along

the curves. The same trend occurs for the 1 M LiBr-ACN SCs (Fig. S3a) and the 1 M LiBr-DMSO SCs (Fig. S4a). The CV curves of the LiBr-PC/ACN/DMSO electrolytes do not exhibit distinct redox peaks in the electrochemical profiles, suggesting that only ion adsorption/desorption contributes to the capacitance in the SCs. The GCD curves of the LiBr-PC/ACN/DMSO electrolyte-based SCs at a current density of 1.0 A g^{−1}, as depicted in Figs. S2b, S3b, and S4b, exhibit the isosceles triangle shape consistently. This observation further confirms that the LiBr-PC/ACN/DMSO electrolyte-based SCs exclusively manifests the characteristics associated with EDLCs.

To enhance the voltage of LiBr-PC/ACN/DMSO electrolyte-based supercapacitors, the hybrid electrolyte comprising 1 M ionic liquid EMIMBF₄ was incorporated into the aforementioned LiBr-PC, LiBr-ACN, and LiBr-DMSO solvents. The CV plots of EMIMBF₄-LiBr-PC and EMIMBF₄-LiBr-ACN SCs were conducted with a scan rate of 10 mV s^{−1}, covering the voltage range from 1.2 to 2.0 V, as depicted in Fig. S5a-b. It is evident that both electrolytes demonstrate rectangular-shaped CV curves below 1.4 V, indicating the double-layer characteristics of the capacitors. However, beyond 1.4 V, the CV curves deviate from their initial rectangular shape. However, the cyclic voltammetry (CV) curves of the EMIMBF₄-LiBr-DMSO SCs exhibit a rectangular shape at operating voltages below 1.1 V when scanned at a rate of 10 mV s^{−1} (Fig. S5c). At this time, the supercapacitor mainly relies on the electric double layer to store energy. When the operating voltage reaches the redox potential of Br[−], the rectangular frame begins to deform, and a wide peak appears on the curve, representing the redox reaction. As the operating voltage increases, the response of the oxidation/reduction peak increases with the corresponding current. The redox reaction of Br[−]/Br₃[−] is initiated at the redox potential when the operating voltage reaches 1.1 V, providing evidence for this phenomenon.

Fig. 2a describes the CV curves of EMIMBF₄-LiBr-PC, EMIMBF₄-LiBr-ACN and EMIMBF₄-LiBr-DMSO SCs at 10 mV s^{−1}. In the CV plots of the hybrid electrolyte, the rectangular region can be observed at voltage levels below 1.1 V, indicating the involvement of the activated carbon electrode in the EDLC process. However, the CV curves of EMIMBF₄-LiBr-PC and EMIMBF₄-LiBr-ACN SCs show obvious voltage boost and

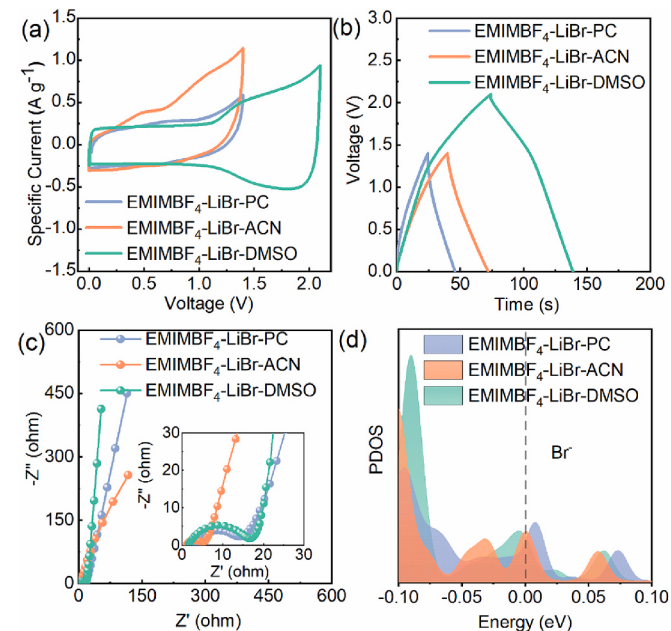


Fig. 2. (a) CV curves, (b) GCD curves and (c) Nyquist plots of EMIMBF₄-LiBr-PC, EMIMBF₄-LiBr-ACN and EMIMBF₄-LiBr-DMSO SCs. (d) Projected density of states (PDOS) (with an arbitrary unit) of the Br[−] in EMIMBF₄-LiBr-PC, EMIMBF₄-LiBr-ACN and EMIMBF₄-LiBr-DMSO electrolyte, respectively. The Fermi level is set to 0 eV in the PDOS analysis.

redox peaks. The analysis in Figs. S2–4 reveals that in the presence of only LiBr and solvent, the LiBr-PC/ACN/DMSO electrolytes do not exhibit redox characteristics, and polarization occurs at a voltage below 2 V. After the introduction of the ionic liquid, a noticeable redox reaction occurs between $\text{Br}^-/\text{Br}_3^-$ in DMSO, resulting in a significant increase in the voltage of the SCs. This observation suggests that within the LiBr-PC/ACN/DMSO electrolyte system, the solvent does not impose limitations on voltage; rather, it is the presence of LiBr that restricts its potential. In this context, LiBr emerges as a crucial redox mediator in hybrid electrolytes, characterized by excellent solubility and electrochemical stability. Beyond its role as an ion source, it actively engages in the indispensable $\text{Br}^-/\text{Br}_3^-$ redox reactions, vital for the energy storage mechanism of supercapacitors. These reactions facilitate rapid charge transfer between the anode and cathode, ensuring swift energy storage and release processes. The voltage of pure EMIMBF₄ can reach >3 V, which is greater than the voltage of LiBr in the solvent, so the increase of the voltage of the hybrid electrolytic liquid system can be attributed to the role of EMIMBF₄.

According to previous reports, solvation emerges as the predominant factor influencing the kinetics of halogen ions within carbon pores [43,44]. Bromine ions exhibit distinct solvation structures in various solvents, leading to variations in the size of their respective solvation shells and consequently affecting their ability to penetrate carbon pore sizes. After the addition of BF₄⁻, the kinetics of Br⁻ in DMSO exhibit distinct deviations from those observed in ACN and PC. This discrepancy arises due to the challenging replacement of solvation structures between PC/ACN-Br⁻ and PC/ACN-BF₄⁻ within the carbon aperture, resulting in no significant increase in voltage. Conversely, DMSO-Br⁻ readily undergoes solvation structure replacement by BF₄⁻ at the carbon aperture, leading to a substantial enhancement in voltage. Consequently, DMSO-BF₄⁻ displaces DMSO-Br⁻ upon entering the carbon electrode aperture, thereby reducing the bonding strength of DMSO-Br⁻ within this region and facilitating redox reactions involving $\text{Br}^-/\text{Br}_3^-$. DMSO's exceptional performance as an organic solvent in bromine-based redox electrochemical double-layer capacitors can be attributed to its remarkable solubility, polarity/solvent polarization effects, high conductivity, and solution stability, collectively contributing to its extraordinary properties. Fig. 2b depicts the GCD curves of SCs based on EMIMBF₄-LiBr-PC, EMIMBF₄-LiBr-ACN and EMIMBF₄-LiBr-DMSO at 1.0 A g⁻¹. The GCD curves of the EMIMBF₄-LiBr-PC and EMIMBF₄-LiBr-ACN SCs exhibit typical double layer characteristics. However, the clear platform of the GCD curve of EMIMBF₄-LiBr-DMSO SCs at about 1.1 V can be attributed to the redox reaction occurring in $\text{Br}^-/\text{Br}_3^-$, which indicates that the introduction of bromine ions in EMIMBF₄-DMSO can increase the pseudocapacitance contribution.

To further study the performance of the SCs, the results of EIS measurement are shown in Fig. 2c. The three EIS curves have the same shape characteristics, namely, the semicircular arc in the high frequency region and the edge in the low frequency region. The diameter of the semicircle represents the charge transfer resistance between the electrolyte and the electrode interface, while the linear segment depicts the capacitance characteristic. The straight line represents the capacitance characteristic. EMIMBF₄-LiBr-DMSO SCs linear slope ratio EMIMBF₄-LiBr-PC and the EMIMBF₄-LiBr-ACN SCs are large, which indicates that the ion diffusion speed of the EMIMBF₄-LiBr-DMSO SCs is faster, relatively fast kinetics and good electrochemical behavior. To further investigate the charge storage behavior of Br⁻ in three electrolyte systems, we have computed the partial density of states (PDOS) for these systems. The increased integral area of the PDOS indicates a higher abundance of electronic states available for redox reactions within the system. Fig. 2d illustrates the partial density of states (PDOS) for three electrolyte systems, indicating that under identical conditions, the EMIMBF₄-LiBr-DMSO system with the highest number of oxidized electrons (activity) exhibits more effective Br oxidation-reduction behavior. Consequently, it can be inferred that this system demonstrates enhanced activity under comparable conditions, thereby

promoting a more efficient Br oxidation-reduction reaction.

The above analysis indicates that DMSO serves as the optimal inert solvent for SCs in this study. To attain optimal electrochemical performance of LiBr redox additives in hybrid electrolyte systems, the impact of redox additive concentration on electrochemical performance was investigated. The electrochemical performance testing involved LiBr concentrations ranging from 0 M to 1.0 M, as illustrated in Fig. S6. The absence of a redox peak at low LiBr concentrations (0–0.8 M) suggests that the equilibrium state between the redox medium and solvent has not been optimally established. The appearance of a pair of oxidation-reduction peaks around a potential of 1.5 V, when the concentration of LiBr reaches 1 M, signifies the optimal concentration. When the concentration of LiBr is 0–0.8 M, GCD profiles all show the quasi-triangle, indicating that within this concentration range, the supercapacitor still follows the charge and discharge mechanism of EDLC, while when the concentration of LiBr is 1 M, the GCD profiles deviates from the quasi-triangle shape, indicating that there is a Faradaic charge storage mechanism at this time. Fig. S7 shows the specific capacitance values corresponding to different LiBr concentrations calculated according to the gcd diagram. It can be seen that when the LiBr concentration reaches 1 M, the specific capacitance is the highest (35.17 F g⁻¹).

Therefore, it is necessary to conduct further research on the EMIMBF₄-LiBr-DMSO SCs. The CV curves of EMIMBF₄-LiBr-DMSO SCs at different scan rates are illustrated in Fig. 3a, while maintaining an operational voltage of 2.5 V. The distribution of CV curves remain stable across the large sweep rate range of 10 to 100 mV s⁻¹ large sweep rate, indicating a robust current response and confirming the excellent capacitive and pseudocapacitive behavior of the EMIMBF₄-LiBr-DMSO SCs. As the scanning rate increases, the combined effect of ionic resistance and electronic resistance under polarization causes a negative shift in the reduction peak. The detailed contributions of diffusion limits and capacitive control are depicted in Fig. S8a. At a scanning rate of 10 mV s⁻¹, the contribution from capacitance is measured to be 71.24 %, with the portion controlled by capacitance gradually increasing as the scanning rate rises. The b values for the redox supercapacitors all close to 1 (Fig. S8b), indicating that redox capacitance control governs the entire reaction process. The GCD curves also demonstrate a triangular shape at various current densities, further confirming the excellent reversibility and rate capability of the SCs (Fig. 3b). Figs. 3c and S9 depict the capacitance values of the supercapacitor at scan rates ranging from 10 to 100 mV s⁻¹. At a scanning rate of 10 mV s⁻¹, the specific capacitance of the EMIMBF₄-DMSO supercapacitor is 24.86 F g⁻¹ (38.28 F cm⁻³), while the EMIMBF₄-LiBr-DMSO supercapacitor exhibits a specific capacitance of 39.72 F g⁻¹ (61.17 F cm⁻³), representing a 159 % increase compared to the specific capacitance of the EMIMBF₄-DMSO supercapacitor without the addition of a redox medium. Even at a large scan rate of 100 mV s⁻¹, the EMIMBF₄-LiBr-DMSO redox SCs can still reach the specific capacitance of 26.10 F g⁻¹ (40.19 F cm⁻³), and the capacitance retention is 65.71 %. Fig. 3d is Ragone plots based on EMIMBF₄-LiBr-DMSO and EMIMBF₄-DMSO carbon-based symmetric SCs. The EMIMBF₄-LiBr-DMSO redox SCs have an energy density of 34.48 Wh kg⁻¹ at a power density of 496.6 W kg⁻¹. Even when operating at high power densities up to 3262.1 W kg⁻¹, their energy density remains relatively high at 22.65 Wh kg⁻¹, surpassing previously reported SCs [1,3,45–51] (Table S2). In comparison, the EMIMBF₄-DMSO SCs show an energy density ranging from 21.58 Wh kg⁻¹ to 17 Wh kg⁻¹ within the power density range of 310.8 W kg⁻¹ to 2581.5 W kg⁻¹. After adding LiBr redox medium, the power density and energy density of EMIMBF₄-LiBr-DMSO redox SCs are increased compared with EMIMBF₄-DMSO SCs. To further evaluate the cycling performance of the EMIMBF₄-LiBr-DMSO redox SCs, we conducted 8000 cycles of GCD measurements on the device under a current density of 1 A g⁻¹. (Fig. 3e). After 8000 cycles, the capacitance retention of the redox supercapacitor is 70.58 %, and the Coulombic efficiency increases from 71.78 % to 99.39 %. The self-discharge curve of the redox supercapacitor shown in Fig. S10

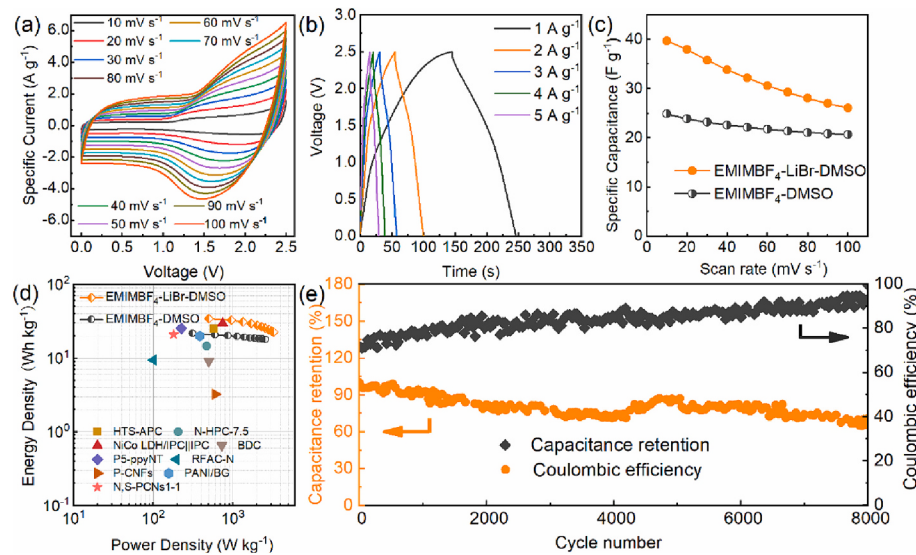


Fig. 3. (a) CV curves with different scanning rates and (b) GCD curves with different current densities of EMIMBF₄-LiBr-DMSO SCs. (c) Rate performance and (d) Ragone plots of EMIMBF₄-LiBr-DMSO and EMIMBF₄-DMSO SCs. (e) Cycle life diagram of EMIMBF₄-LiBr-DMSO SCs at 1 A g⁻¹.

demonstrates that even after 15,000 s, the open circuit voltage remains stable at approximately 0.6 V, thereby confirming its suitability as a reliable power source.

The nitrogen adsorption/desorption experiments were conducted to analyze the YP-50F activated carbon's BET surface area and pore structure. It can be observed from Fig. S11a that YP-50F demonstrates a significant rise in gas adsorption volume at low pressures (relative pressure $P/P_0 = 0.0\text{--}0.1$), suggesting the presence of a considerable number of micropores within YP-50F. The hysteresis ring observed in the P/P_0 range of 0.5–0.8 clearly suggests a relatively closed pore structure or rough inner pore walls. The observed increase in gas adsorption within this range suggests the presence of abundant mesopores in YP-50F. It is evident that YP-50F possesses a specific surface area measuring 1364.72 m² g⁻¹, accompanied by an average aperture size of 2.213 nm. The pore size distribution of YP-50F, depicted in Fig. S11b, reveals predominant sizes around 0.7, 1.2, and 1.5 nm, aligning with the findings derived from the analysis of the nitrogen absorption/desorption curve.

In order to further explore the influence of electrolyte on performance, FTIR and XPS were used to analyze the elemental composition of carbon materials and non-recycled carbon materials after cycling in EMIMBF₄-LiBr-PC, EMIMBF₄-LiBr-ACN and EMIMBF₄-LiBr-DMSO electrolyte. The surface functional groups of the carbon electrode before and after cycling were further elucidated by recording and comparing the FTIR spectra of each electrolyte. As illustrated in Fig. 4a, there is no significant modification in the functional groups on the electrode surface, suggesting a high degree of reversibility. XPS spectra shows that there are four signal peaks of C 1 s (284.8 eV), N 1 s (400.2 eV), O 1 s (531.5 eV) and F 1 s (686.1 eV) in carbon materials before and after the cycle (Fig. 4b). The analysis indicates that the carbon material contains elements such as C, N, O, and F. The presence of the F element can be attributed to the binder polytetrafluoroethylene, while the N element is derived from activated carbon's raw plant fiber (Fig. S12). Interestingly, Br (69.1 eV) signal peaks appeared in both EMIMBF₄-LiBr-PC and EMIMBF₄-LiBr-ACN electrolyte cycles, indicating that the solvation structure of PC/ACN-Br⁻ was bound to the electrode's pore structure during the reaction process. Despite the presence of PC/ACN-BF₄⁻ in the system, it is unable to substitute PC/ACN-Br⁻ within the pore size, thereby hindering complete redox reaction of Br⁻/Br₃⁻, which aligns with the aforementioned electrochemical behavior. The absence of Br element in the carbon material after the EMIMBF₄-LiBr-DMSO cycle can be attributed to the replacement of DMSO-Br⁻ solvation structure by

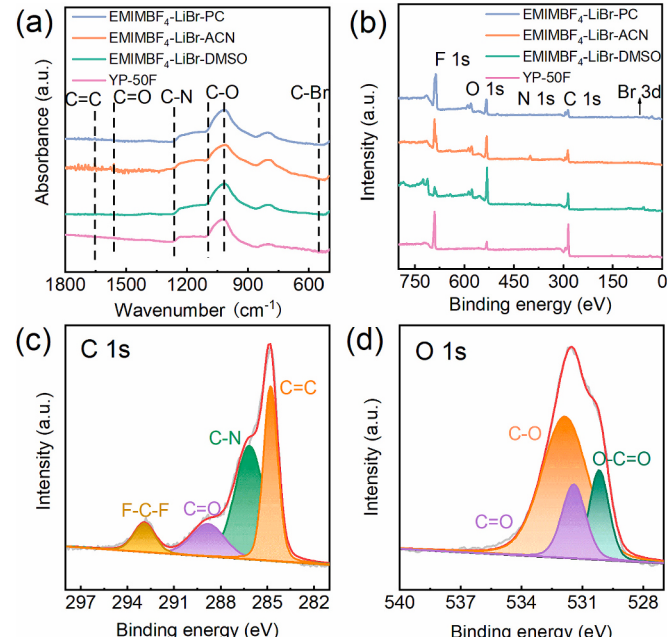


Fig. 4. (a) FTIR spectra, (d) XPS full spectrum of carbon materials and non-recycled carbon materials after cycling in EMIMBF₄-LiBr-PC, EMIMBF₄-LiBr-ACN and EMIMBF₄-LiBr-DMSO electrolyte. High-resolution XPS spectra of (c) C 1s and (d) O 1s of carbon materials after cycling in EMIMBF₄-LiBr-DMSO electrolyte.

DMSO-BF₄⁻. Subsequently, when DMSO-BF₄⁻ replaces DMSO-Br⁻ within the electrode aperture, it facilitates the reduction of DMSO-Br⁻ binding in carbon pores, enabling the occurrence of Br⁻/Br₃⁻ redox reaction. This electrochemical behavior is characterized by an increased pseudocapacitance resulting from Faraday reaction of the redox pair. The high-resolution C 1 s spectrum of carbon materials after cycling in EMIMBF₄-LiBr-DMSO electrolyte, as depicted in Fig. 4c, exhibits four distinct component peaks: C=C (284.6 eV), C=N (286.2 eV), C=O (289.1 eV) and F-C-F (292.1 eV). Similarly, the O-1 s spectrum with high resolution can be separated into three separate component peaks (Fig. 4d): O=C-O (530.1 eV), C=O (531.4 eV), and C—O (531.8 eV).

4. Conclusions

In summary, we used three different organic solvents as inert solvents, EMIMBF₄ as ionic liquid and LiBr as redox reaction medium to prepare redox electrolyte. ACN, PC and DMSO are all organic solvents with high dielectric constant, which can effectively dilute the ionic liquid to improve the electrolyte's ionic conductivity. The LiBr redox pair, consisting of Br⁻/Br₃⁻, exhibits a standard high potential, excellent solubility, and rapid reaction kinetics. The investigation identified that the EMIMBF₄-LiBr-DMSO electrolyte system stands out as the most favorable liquid system for EDLCs in this work, owing to its optimal electrochemical properties. The redox SCs utilizing EMIMBF₄-LiBr-DMSO exhibit a specific capacitance of 39.72 F g⁻¹, along with a high power density of 496.6 W kg⁻¹, and simultaneously attain an energy density of 34.48 Wh kg⁻¹. This work provides a new approach for developing high-performance redox electrolytes, which contributes to the advancement of bromine-based supercapacitors in the field of energy storage.

CRediT authorship contribution statement

Zhemin Li: Writing – original draft, Conceptualization, Investigation, Formal Analysis. **Dewei Xiao:** Investigation, Formal analysis. **Zihan Li:** Methodology, Data curation. **Zhenming Xu:** Validation, Formal analysis. **Hui Dou:** Writing – review & editing, Project administration. **Xiaogang Zhang:** Writing – review & editing, Supervision, Funding acquisition, Conceptualization.

Declaration of competing interest

The authors declare that they have no known competing financial interests or personal relationships that could have appeared to influence the work reported in this paper.

Data availability

Data will be made available on request.

Acknowledgments

This work was supported by the National Natural Science Foundation of China (2022YFE0109400), National Key Research and Development Program of China (2023YFB2405800), Leading Edge Technology of Jiangsu Province (BK20220009) and Priority Academic Program Development of Jiangsu Higher Education Institutions (PAPD). The authors acknowledge the facilities in the Center for Microscopy and Analysis at Nanjing University of Aeronautics and Astronautics.

Appendix A. Supplementary data

Supplementary data to this article can be found online at <https://doi.org/10.1016/j.est.2024.111735>.

References

- [1] Z. Liu, C. Duan, S. Dou, Q. Yuan, J. Xu, W.D. Liu, Y. Chen, Small 18 (2022) e2200954.
- [2] S. Wu, B. Su, M. Sun, S. Gu, Z. Lu, K. Zhang, D.Y.W. Yu, B. Huang, P. Wang, C. S. Lee, W. Zhang, Adv. Mater. 33 (2021) 202102390.
- [3] F. Sun, Z. Qu, J. Gao, H.B. Wu, F. Liu, R. Han, L. Wang, T. Pei, G. Zhao, Y. Lu, Adv. Funct. Mater. 28 (2018) 1804190.
- [4] Y. Shao, M.F. El-Kady, J. Sun, Y. Li, Q. Zhang, M. Zhu, H. Wang, B. Dunn, R. B. Kaner, Chem. Rev. 118 (2018) 9233–9280.
- [5] F. Xing, Z. Bi, F. Su, F. Liu, Z.S. Wu, Adv. Energy Mater. 12 (2022) 2200594.
- [6] Y. Wang, Y. Song, Y. Xia, Chem. Soc. Rev. 45 (2016) 5925–5950.
- [7] J. Zhou, H.-Y. Hu, H.-Q. Li, Z.-P. Chen, C.-Z. Yuan, X.-J. He, Rare Metals 42 (2022) 719–739.
- [8] M. Sevilla, R. Mokaya, Energy Environ. Sci. 7 (2014) 1250–1280.
- [9] B. Li, F. Dai, Q. Xiao, L. Yang, J. Shen, C. Zhang, M. Cai, Energy Environ. Sci. 9 (2016) 102–106.
- [10] S. Hu, R. Rajamani, X. Yu, Appl. Phys. Lett. 100 (2012).
- [11] T. Chen, L. Dai, Mater. Today 16 (2013) 272–280.
- [12] J. Yu, W. Lu, S. Pei, K. Gong, L. Wang, L. Meng, Y. Huang, J.P. Smith, K.S. Booksh, Q. Li, J.-H. Byun, Y. Oh, Y. Yan, T.-W. Chou, ACS Nano 10 (2016) 5204–5211.
- [13] L.L. Zhang, R. Zhou, X.S. Zhao, J. Mater. Chem. 20 (2010) 5983–5992.
- [14] C. Liu, Z. Yu, D. Neff, A. Zhamu, B.Z. Jang, Nano Lett. 10 (2010) 4863–4868.
- [15] T. Kim, G. Jung, S. Yoo, K.S. Suh, R.S. Ruoff, ACS Nano 7 (2013) 6899–6905.
- [16] J.R. Miller, P. Simon, Science 321 (2008) 651–652.
- [17] Q. Gou, S. Zhao, J. Wang, M. Li, J. Xue, Nano Lett. 12 (2020) 98.
- [18] Y. Zheng, D. Wang, S. Kaushik, S. Zhang, T. Wada, J. Hwang, K. Matsumoto, R. Hagiwara, EnergyChem 4 (2022) 100075.
- [19] A. Lewandowski, A. Olejniczak, J. Power Sources 172 (2007) 487–492.
- [20] V. Ruiz, T. Huynh, S.R. Sivakkumar, A.G. Pandolfo, RSC Adv. 2 (2012) 5591–5598.
- [21] R. Palm, H. Kurig, K. Tönurist, A. Jänes, E. Lust, J. Electrochem. Soc. 160 (2013) A1741–A1745.
- [22] N.A. Thu Tran, N.M. Phuoc, H. Yoon, E. Jung, Y.-W. Lee, B.-G. Kang, H.S. Kang, C.-Y. Yoo, Y. Cho, ACS Sustain. Chem. Eng. 8 (2020) 16701–16710.
- [23] H. Tang, Y. Liang, C. Liu, Z. Hu, Y. Deng, H. Guo, Z. Yu, A. Song, H. Zhao, D. Zhao, Y. Zhang, X. Guo, J. Pei, Y. Ma, Y. Cao, F. Huang, Nature 611 (2022) 271–277.
- [24] J.S. Bates, S. Biswas, S.-E. Suh, M.R. Johnson, B. Mondal, T.W. Root, S.S. Stahl, J. Am. Chem. Soc. 144 (2022) 922–927.
- [25] P. Yang, T. Jiang, Z. Cong, G. Liu, Y. Guo, Y. Liu, J. Shi, L. Hu, Y. Yin, Y. Cai, G. Jiang, Environ. Sci. Technol. 56 (2022) 6744–6753.
- [26] M. Chang, D. Liang, F. Zhou, H. Xue, H. Tong, W. Chen, G. Zhou, A.C.S. Appl. Mater. Inter. 14 (2022) 15448–15460.
- [27] Y. Sun, Q. Zou, Y.-C. Lu, Adv. Energy Mater. 9 (2019) 1903002.
- [28] X. Lang, Y. Huang, L. He, Y. Wang, U. Thumu, Z. Chu, W.T.S. Huck, H. Zhao, Nat. Commun. 14 (2023) 3084.
- [29] B.Y. Wen, J.-S. Lin, Y.-J. Zhang, P.M. Radjenovic, X.-G. Zhang, Z.-Q. Tian, J.-F. Li, J. Am. Chem. Soc. 142 (2020) 11698–11702.
- [30] M. Nan, M. Wu, Y. Liu, L. Qiao, H. Zhang, X. Ma, Small Methods 7 (2022) 2201266.
- [31] T. Ouyang, B. Jin, Y. Mao, D. Wei, Z. Liang, Appl. Catal. B Environ. 343 (2024) 123531.
- [32] R. Xie, D. Yue, Z. Peng, X. Wei, Energy Mater. Adv. 4 (2023) 0009.
- [33] J.H. Lin, X.S. Du, Chem. Eng. J. 446 (2022) 137244.
- [34] C. Hu, Y. Qin, Z. Song, P. Liu, L. Miao, H. Duan, Y. Lv, L. Xie, M. Liu, L. Gan, J. Colloid Interface Sci. 658 (2024) 856–864.
- [35] M. Cui, N. Ma, H. Lei, Y. Liu, W. Ling, S. Chen, J. Wang, H. Li, Z. Li, J. Fan, Y. Huang, Angew. Chem. Int. Ed. 62 (2023) e202303845.
- [36] Q. Han, S. Wang, L. Wang, W. Ren, F. Zhang, J. Lu, H. Wang, Adv. Energy Mater. 13 (2023) 2301462.
- [37] Y. Yang, S. Guo, Y. Pan, B. Lu, S. Liang, J. Zhou, Energy Environ. Sci. 16 (2023) 2358–2367.
- [38] W. Du, L. Miao, Z. Song, X. Zheng, C. Hu, Y. Lv, L. Gan, M. Liu, Chem. Eng. J. 484 (2024) 149535.
- [39] W. Ma, T. Liu, C. Xu, C. Lei, P. Jiang, X. He, X. Liang, Nat. Commun. 14 (2023) 5508.
- [40] Y. Zhao, M. Duan, C. Deng, J. Yang, S. Yang, Y. Zhang, H. Sheng, Y. Li, C. Chen, J. Zhao, Nat. Commun. 14 (2023) 1943.
- [41] Y. Zhang, Z. Song, L. Miao, Y. Lv, L. Gan, M. Liu, Angew. Chem. Int. Ed. 63 (2023) e202316835.
- [42] T.J.D. Souza Ramos, G.H. Berton, T.M. Cassol, S.A. Júnior, J. Mater. Chem. C 6 (2018) 6270–6279.
- [43] Q. Zhang, Y. Ma, Y. Lu, Y. Ni, L. Lin, Z. Hao, Z. Yan, Q. Zhao, J. Chen, J. Am. Chem. Soc. 144 (2022) 18435–18443.
- [44] R. Hou, Y. Wang, Y. Sun, J. Lang, S. Yang, X. Yan, Nano Energy 99 (2022) 107377.
- [45] Y. Liu, J. Zhou, L. Chen, P. Zhang, W. Fu, H. Zhao, Y. Ma, X. Pan, Z. Zhang, W. Han, E. Xie, A.C.S. Appl. Mater. Inter. 7 (2015) 23515–23520.
- [46] Q. Hao, X. Xia, W. Lei, W. Wang, J. Qiu, Carbon 81 (2015) 552–563.
- [47] B. Du, L. Huang, M. Shen, H. Zhou, B. Wang, Z. Deng, L. Wang, D. Nie, Energy Fuel 35 (2021) 18789–18797.
- [48] J. Gu, H. Wang, S. Li, M. Sohail Riaz, J. Ning, X. Pu, Y. Hu, J. Colloid Interface Sci. 635 (2023) 254–264.
- [49] X. Zhang, Q. Lu, E. Guo, J. Feng, M. Wei, J. Ma, J. Energy Storage 38 (2021) 102514.
- [50] X. Luo, Q. Yang, Y. Dong, X. Huang, D. Kong, B. Wang, H. Liu, Z. Xiao, L. Zhi, J. Mater. Chem. A 8 (2020) 17558–17567.
- [51] Y. Li, G. Wang, T. Wei, Z. Fan, P. Yan, Nano Energy 19 (2016) 165–175.